


## Prediction of Self-Assembled Dewetted Nanostructures for Photonics Applications via a Continuum-Mechanics Framework

L. Martin-Monier<sup>1,‡</sup>, P. G. Ledda<sup>2,‡</sup>, P. L. Piveteau,<sup>1</sup> F. Gallaire,<sup>2,\*</sup> and F. Sorin<sup>1,†</sup>

<sup>1</sup>Laboratory of Photonic Materials and Fiber Devices, IMX, École Polytechnique Fédérale de Lausanne, 1015 Lausanne, Switzerland

<sup>2</sup>Laboratory of Fluid Mechanics and Instabilities, IGM, École Polytechnique Fédérale de Lausanne, 1015 Lausanne, Switzerland

 (Received 30 April 2021; revised 6 July 2021; accepted 12 August 2021; published 14 September 2021)

When a liquid film lies on a nonwetable substrate, the configuration is unstable, and the film spontaneously ruptures to form droplets. This phenomenon, known as dewetting, commonly leads to undesirable morphological changes. Nevertheless, recent works, combining spontaneous dewetting triggered by thermal annealing and topographic pattern-directed dewetting, demonstrate the possibility of harnessing dewetting with a degree of precision on par with that of advanced lithographic processes for high-performance nanophotonic applications. Since resonant behavior is highly sensitive to geometrical changes, predicting quantitatively dewetting dynamics is of high interest. Here, we develop a continuum model that predicts the evolution of a thin film on a patterned substrate, from the initial reflow to the nucleation and growth of holes. We provide an operative framework based on macroscopic measurements to model the intermolecular interactions at the origin of the dewetting process, involving length scales that span from sub-nanometer to micrometer. A comparison of experimental and simulated results shows that the model can accurately predict the final distributions, thereby offering predictive tools to tailor the optical response of dewetted nanostructures.

DOI: [10.1103/PhysRevApplied.16.034025](https://doi.org/10.1103/PhysRevApplied.16.034025)

### I. INTRODUCTION

Flows of thin films over substrates are of central interest, owing to their ubiquity in natural and industrial environments. Depending on the interactions between the film, substrate, and surrounding environment, thin films with sufficient mobility may dewet either through spontaneous amplification of surface perturbations (spinodal dewetting) or through nucleation and growth of holes. The ruptured holes grow due to an imbalance in the component of surface tension tangential to the substrate at the contact line and often the growing holes (or the rims of the growing holes) coalesce, resulting in cellular structures and threads that disintegrate into droplets [1–3]. The miniaturization of modern devices involving ultrathin layers leads to a focus on the question of dewetting. This ubiquitous phenomenon threatens the integrity of thin films, typically yielding semiordered tessellation patterns. This is often an undesirable phenomenon, jeopardizing the film morphology with little practical use. Nevertheless, the potential

of dewetting is investigated as an efficient self-assembly process with several technologically relevant applications, such as water harvesting [4], the fabrication of water-stable photodetectors [5], or peptide self-assembly [6]. Recent works have also highlighted the possibility of exploiting the resulting dewetted patterns for their tailored scattering properties [7]. Resorting to high-index dielectric glasses has relevance in nanophotonics [7], where the control of the nanoresonator geometry allows for wide engineering of scattering and resonant properties. Several approaches to induce order through pattern-directed dewetting have been proposed, either based on chemical [8,9] or topographic modulation [10–13] of the substrate. These investigations have demonstrated interesting possibilities but remain limited in terms of materials, scalability, geometry, or resolution. By combining engineered substrates with functional materials, dewetting triggered by thermal annealing has emerged as a viable alternative [14–17], as illustrated in Fig. 1. In opposition to mono- or polycrystalline solid thin films that dewet according to surface-diffusion mechanisms [18,19], viscous thin films dewet following bulky viscous-flow mechanisms. Such dewetting processes in fluid thin films can be triggered in several ways [20], such as a solvent-vapor exposure or thermal annealing above the glass transition temperature [2], as introduced above.

\* francois.gallaire@epfl.ch

† fabien.sorin@epfl.ch

‡ L. Martin-Monier and P. G. Ledda contributed equally to this work.

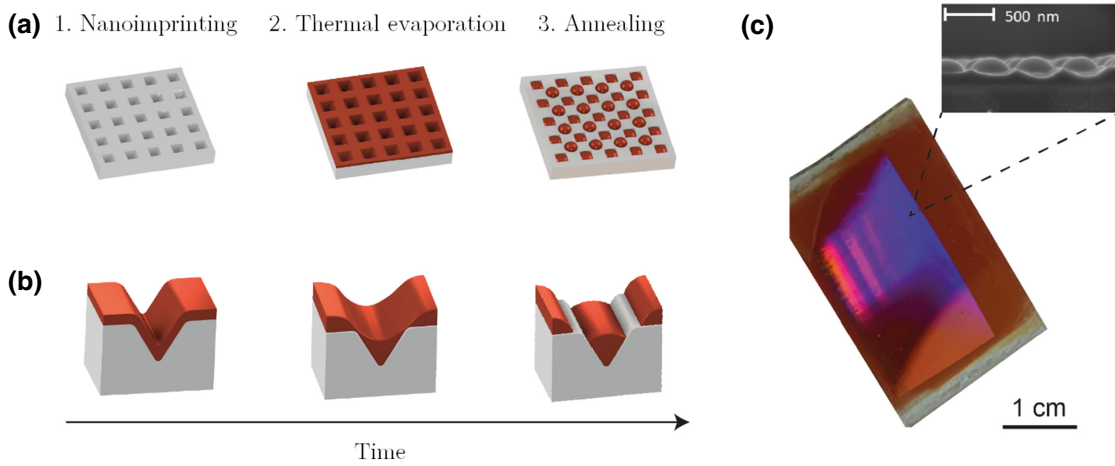


FIG. 1. Description of dewetting triggered by thermal annealing. (a) Schematic describing the three main process steps: (1) nanoimprinting of a nanoscale texture onto a sol-gel or UV-curable substrate from a silicon master mold, (2) thermal evaporation of a thin ( $<100$  nm) optical glass layer, and (3) dewetting triggered by thermal annealing above the glass transition temperature. Dewetting process induces an ordered rearrangement of the film, according to the underlying texture. (b) Time evolution of the thin viscous film during dewetting. (c) Optical photograph of a 350-nm meta-array of selenium nanoparticles.

While surface diffusion of solid thin films over templates has been the object of several investigations [14,18,21,22], the flow of viscous films over prepatterned substrates has thus far only been the object of linear stability analysis, which fails to predict the complete dewetting dynamics [23,24]. This is surprising, as isotropic material properties associated with a viscous fluid allow for improved control of the rearrangement mechanism and higher complexity in the final microstructures. This is particularly relevant in nanophotonics, where changes in feature size to as little as 10 nm can strongly impact on the resonant behavior and the resulting optical properties. To increase the method's accuracy and further extend its realm of application, prediction, in the most precise manner, of the final microstructure based on the exact substrate shape and film-substrate interactions is of paramount importance, which motivates the present study. Several numerical approaches are possible to study the dynamics of a liquid thin film. Since molecular simulations are still too complex numerically, approaches based either on Monte Carlo [25–28] or continuum models, such as the Navier-Stokes equations, may be preferably used [29–33]. The latter are often based on phase-field or volume-of-fluid approaches [30–32], so as to simulate the two liquid phases and the solid-phase interactions involved in the dynamics. The interaction with the solid phase leads to a stress singularity to be regularized at the moving contact line, where nanometer-scale interactions become predominant [34]. Typical approaches are based on slip-velocity boundary conditions [29,31,32] or on the introduction of an intermolecular potential into the flow equations [33,35]. An alternative to the above-mentioned models is the so-called long-wave or lubrication approximation. The latter allows for the reduction

of the Navier-Stokes equations to a single equation for fluid thickness [36,37]. While initially developed for thin films with small slopes, lubrication models also show great potential in the case of large slopes, and thus, for problems with nonzero contact angles [29]. The contact line can be modeled through a suitable disjoining pressure, which integrates both attractive long-range van der Waals forces and repulsive short-range intermolecular interactions between solid and fluids [1,2].

Intertwining spontaneous dewetting of ultrathin optical glass films by thermal annealing [2] with topographic pattern-directed dewetting [10,12,13] offers some unique yet unexploited opportunities to create nanostructures with tailored optical properties, with a very large set of applications in the realm of nanophotonics. Herein, we propose a continuum model that predicts the evolution of a templated film evolving over prepatterned substrates, based on the modeling of intermolecular interactions occurring on various substrates, for contact angles less than  $90^\circ$ . By comparing experimental and simulated thickness profiles over various patterns, we show that the proposed model is suitable for the accurate prediction of the final morphology and over several length scales (from nm to  $\mu\text{m}$  scale). We thereby offer improved control of the dewetting patterns, allowing for the realization of precise architectures relevant to nanophotonics.

## II. MODEL DESCRIPTION

### A. Dewetting on flat substrates: Validation

An accurate dynamic description of dewetting constitutes a particularly challenging problem. The theoretical framework for the description of fluid flow is based on

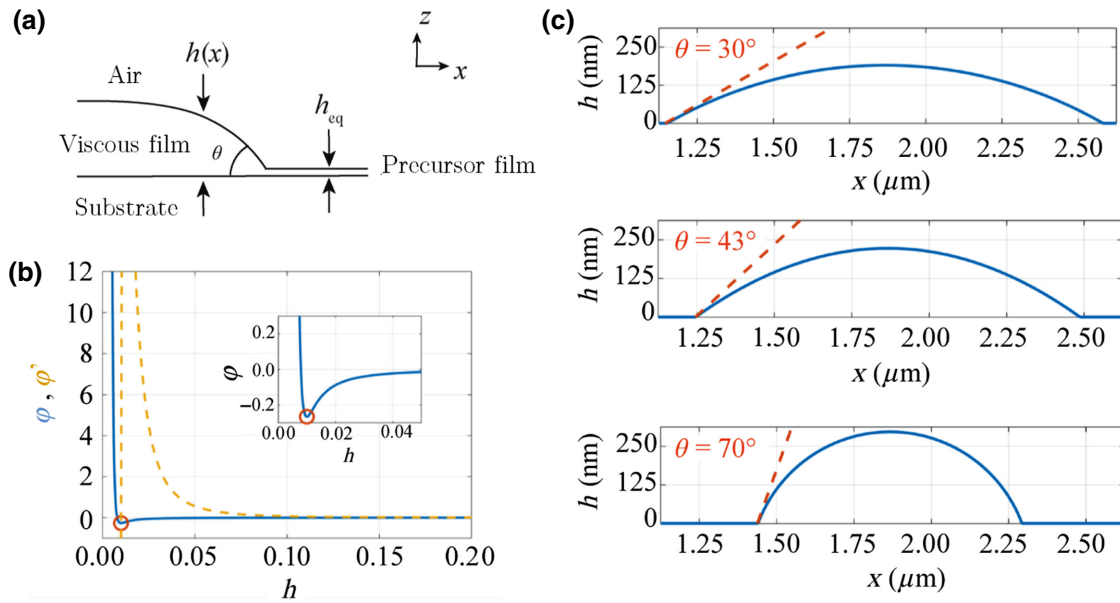


FIG. 2. Precursor film approach implemented on flat substrates. (a) Schematic describing the components of the system and associated parameters in the precursor-film approach. (b) Lennard-Jones potential associated with the viscous film on a flat substrate. Potential (blue curve) shows a minimum, which is further indicated by its derivative (dashed yellow curve) and by the magnification in the inset. Minimum potential corresponds to a film thickness that coincides with the precursor film thickness,  $h_{\text{eq}}$ , indicated in (a). (c) Comparison of the results of the two-dimensional thin-film model (blue solid lines) and the prediction (orange dashed lines) given by Eq. (4), for  $h_i = 25$  nm and different contact angles reported in the figures. From top to bottom,  $A = 5 \times 10^{-20}$  J;  $1 \times 10^{-19}$  J;  $2.5 \times 10^{-19}$  J.

approaches from continuum mechanics. We initially consider a flat horizontal substrate and introduce a coordinate system,  $(x, y, z)$ , where the  $z$  direction, along which the film thickness is measured, coincides with the vertical one, as sketched in Fig. 2(a). The integration of the Navier-Stokes equations along the  $z$  direction, under the classical assumptions of the long-wavelength approximation [36–38], leads to an evolution equation for the thin-film thickness,  $h$ , in the  $(x, y)$  directions; this is the so-called lubrication or thin-film equation:

$$\frac{\partial h}{\partial t} = -\frac{1}{3\mu} \nabla \cdot \{h^3 \nabla [\gamma \kappa + \Pi(h)]\}, \quad (1)$$

where  $\kappa$  is the free-surface curvature,  $\nabla$  operates in the  $(x, y)$  plane,  $\mu$  is the fluid dynamic viscosity,  $\gamma$  is the surface-tension coefficient between the fluid and air, and  $\Pi$  is the so-called disjoining pressure. In the classical framework of the long-wavelength approximation, the curvature is implemented with its linearized version, i.e.,  $\kappa = \nabla^2 h$ , which holds for small slopes of the film. As discussed later, we resort here to the complete expression of the curvature to properly account for arbitrary height profiles. Notably, since the thickness is a single-valued function of the position, contact angles greater than  $90^\circ$  cannot be described by this model.

The disjoining pressure term is assumed to stem from a classical Lennard-Jones type potential [39–41]:

$$\varphi(h) = \frac{B}{h^8} - \frac{A}{12\pi h^2}, \quad (2)$$

where  $A = A_{123}$  is the so-called Hamaker constant of the system substrate (1), film (2), air (3), and  $B$  is the Born coefficient, which is employed to model, respectively, the molecular long-range attractive and short-range repulsive forces. The combination of a repulsive and an attractive term defines a minimum potential for an equilibrium “precursor” film thickness,  $h_{\text{eq}} = (48\pi B/A)^{1/6}$ , which is obtained by imposing  $\varphi'(h_{\text{eq}}) = 0$  [Fig. 2(b)].

The force derived from the Lennard-Jones potential stems from an imbalance in the interactions between the various constituent molecules. This imbalance is classically embedded in the Hamaker constant,  $A_{123}$ , which establishes the influence of constituent materials in long-range interactions, in the presence of multiple bodies, according to Lifschitz theory [42–45]. The previously introduced Lennard-Jones potential is linked to the disjoining pressure,  $\Pi$ , through

$$\Pi = -\frac{\partial \varphi}{\partial h} = \frac{8B}{h^9} - \frac{A}{6\pi h^3}. \quad (3)$$

A positive Hamaker constant induces destabilizing pressure gradients for films larger than the equilibrium thickness,  $h_{\text{eq}}$ . When a region of the film reaches the precursor-film thickness,  $h_{\text{eq}}$ , the local equilibrium at the interface between the precursor film and the thicker regions defines an apparent contact angle,  $\theta$  [Fig. 2(a)], given by [39,46]

$$1 + \tan^2\theta = \left[ \frac{\varphi(h_{\text{eq}})}{\gamma} + 1 \right]^{-2}. \quad (4)$$

Considering solely angles between  $0^\circ$  to  $90^\circ$ , Eq. (4) provides a bijective relationship between the contact angle and the precursor film  $h_{\text{eq}}$ .

To validate this approach, we now proceed to simulate the evolution of a thin film and evaluate the resulting contact angle. The thin-film equation is implemented with the full expression of the interface curvature [47–51]:

$$\kappa = -\nabla \cdot \mathbf{n}, \quad (5)$$

$$\mathbf{n} = \frac{1}{[1 + (\partial h/\partial x)^2 + (\partial h/\partial y)^2]^{1/2}} \begin{pmatrix} -\frac{\partial h}{\partial x} \\ -\frac{\partial h}{\partial y} \end{pmatrix}, \quad (6)$$

where  $\mathbf{n}$  embeds the  $x$  and  $y$  components of the normal of the fluid-free surface; the problem is completed with the disjoining pressure,  $\Pi(h)$ , detailed above. The model with the full expression of curvature, despite its simplicity, shows very good agreement with various experimental measurements, even for cases in which the typical assumptions of the long-wave approximation are not respected [48]. To verify the consistency of the relationship between equilibrium thickness and contact angle, we perform numerical simulations with the finite-element solver COMSOL Multiphysics by implementing the weak form of Eqs. (1), (3), (5), and (6) in conservative form. We choose three different values of contact angles and three different values of the Hamaker constant and determine the corresponding values of the Born coefficient,  $B$ . We then determine the Born coefficient by using Eqs. (2)–(4). Two-dimensional simulation results (i.e.,  $\partial h/\partial y = 0$ ) with an initial thickness of  $h_i = 25$  nm and  $\gamma = 3 \times 10^{-2}$  N.m $^{-1}$  are shown in Fig. 2(c), for three different values of  $A = 5 \times 10^{-20}$ ,  $1 \times 10^{-19}$ , and  $2.5 \times 10^{-19}$  J. The numerical values of the contact angle match the predicted ones with an accuracy below  $1^\circ$ , which validates the proposed approach on flat substrates. The implementation of the complete curvature is essential to yield proper results. The linearized curvature,  $\kappa = \nabla^2 h$ , in the long-wavelength approximation gives contact-angle values with over  $10^\circ$  error compared with the target value. Despite the small size of the final drop states involved, the importance of the complete curvature expression to recover the final static shape is remarkable.

It is also important to note that the presence of a precursor film implies a loss of volume proportional to the precursor-film thickness. The volume error associated with this choice is in all cases presented here inferior to 1%, and thus neglected.

At this stage, an important question arises for the choice of the contact angle. During dewetting, it is common that contact angles evolve dynamically, owing to the elasticity of the triple line [1]. In this framework, it is observed that the final contact angle does not show a strong dispersion in the final stage of dewetting (inferior to  $6^\circ$ , see Fig. S1 within the Supplemental Material [52]). A hysteresis is thus neglected in the rest of this work. Despite this assumption, our model still allows for a relatively accurate prediction of experimental observations, as discussed below.

In previous works that developed a model based on the Lennard-Jones potential [38,39,41], the contact angle was inferred from accurate Hamaker constant and Born coefficient data, with good agreement between theoretically derived and experimentally measured contact angles. This approach assumes prior knowledge of the Born coefficient, which is significantly harder to quantify than the Hamaker constant, and thus, constitutes a significant limitation for broader use of such a modeling scheme. Moreover, this requires knowledge of the precursor-film thickness, a challenging quantity to experimentally measure (typically in the angstrom range). Here, we propose to use the Born coefficient, and thus, the equilibrium thickness given by Eq. (4), as an independent parameter to match the experimental and modeled contact angles in analogy to the procedure in Fig. 2(c) (see Appendix C). In contrast with previous works, the knowledge of the equilibrium contact angle, Hamaker constant, and surface-tension coefficient is sufficient to effectively model the thin-film dynamics.

## B. Templated dewetting

We now turn to the evolution of a film with fixed contact angle,  $\theta$ , over a prepatterned (or “templated”) substrate, of height profile  $h_s$  measured along the  $z$  direction, starting from the horizontal reference previously introduced [see Fig. 3(a)]. Here, we consider two different types of templates: (i) lines or two-dimensional templates [Fig. 3(b)], characterized by triangular grooves of base  $W$ , period  $P$ , and spacing  $P-W$  along the  $x$  direction and invariant along the direction orthogonal to the periodicity one ( $y$  direction); and (ii) pyramids or three-dimensional templates [Fig. 3(c)], characterized by pyramidal trenches with periodicity  $P$  along both  $x$  and  $y$  directions. We resort to As $_2$ Se $_3$  thin films thermally evaporated on textured UV-curable polymers or silica substrates (see Appendix A for further details of the materials employed). For the templates shown in Fig. 3(a), the fabrication process [7] leads to dewetted patterns invariant along the  $y$  direction.

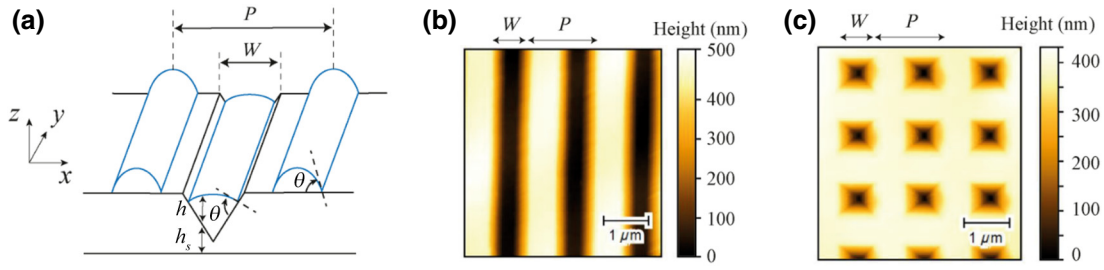


FIG. 3. Two-dimensional and three-dimensional templates. (a) Schematic introducing the contact angle,  $\theta$ ; the film height profile,  $h$ ; the substrate height profile,  $h_s$ ; the inverted pyramid base width,  $W$ ; and the template period,  $P$ . Atomic force microscopy images of textures nanoimprinted on an Ormocomp substrate: (b) triangular grooves (two-dimensional template) and (c) square arrays of inverted pyramids (three-dimensional template).

To accurately predict the thin-film dynamics and the resulting microstructure, the thin-film equation must be adapted to account for the role of the underlying substrate.

The total surface curvature,  $\kappa$ , in this new configuration is now given by the curvature of the total elevation of the free surface ( $h + h_s$ ) [53]:

$$\kappa = -\nabla \cdot \mathbf{n}_t, \quad (7)$$

$$\mathbf{n}_t = \frac{1}{\{1 + [(\partial h/\partial x) + (\partial h_s/\partial x)]^2 + [(\partial h/\partial y) + (\partial h_s/\partial y)]^2\}^{1/2}} \begin{bmatrix} \left(-\frac{\partial h}{\partial x} - \frac{\partial h_s}{\partial x}\right) \\ \left(-\frac{\partial h}{\partial y} - \frac{\partial h_s}{\partial y}\right) \end{bmatrix}. \quad (8)$$

Another difference from the flat-substrate case lies in the definition of the film thickness in the Lennard-Jones potential. Recalling the definition of potential [Eq. (2)], the contact angle depends on the equilibrium thickness. A proper definition of the thickness is therefore crucial to reproduce identical contact angles over the whole substrate. On a flat substrate, thickness is defined straightforwardly as the vertical projection. However, in the case of an underlying inclined substrate, an accurate film thickness is defined as the shortest distance between the film-air interface and the film-substrate, i.e., the projection given by

$$h^* = h \cos \left( \text{atan} \left\{ \left[ \left( \frac{\partial h_s}{\partial x} \right)^2 + \left( \frac{\partial h_s}{\partial y} \right)^2 \right]^{1/2} \right\} \right). \quad (9)$$

To validate the proposed scheme, numerical simulations using experimental atomic scanning microscope profiles of nanoimprinted substrates are performed. We take as initial condition a constant flat thickness that matches the imposed thicknesses in the experimental campaign (see Appendix A). The experimental film profile upon dewetting is then superposed to compare the match between experimental and simulated data. First, investigating the

two-dimensional (2D) case, the experimental and simulated dewetted film profiles are compared in Fig. 4 (period  $2 \mu\text{m}$ , interpyramid spacing  $1.1 \mu\text{m}$ , film thickness  $60 \text{ nm}$ , contact angle  $\theta = 85^\circ$ ). Additional comparative results in the two-dimensional case are provided in the Supplemental Material [52] (see Fig. S2). The numerical scheme is further validated in three dimensions, using a pyramid with largely reduced spacing (interpyramid spacing  $150 \text{ nm}$ ,

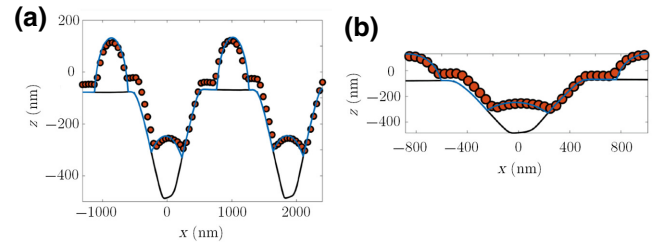


FIG. 4. Simulated vs experimental dewetted profiles in the 2D case. (a) Simulated dewetted profile (blue) and experimental AFM dewetted profile (orange dots) in the case of a  $2\text{-}\mu\text{m}$ -period line pattern with interpyramid spacing  $1.1 \mu\text{m}$  and  $60\text{-nm}$  initial film thickness of  $\text{As}_2\text{Se}_3$ . (b) Magnified view of a single period, showing the match between experimental and simulated contact angles.

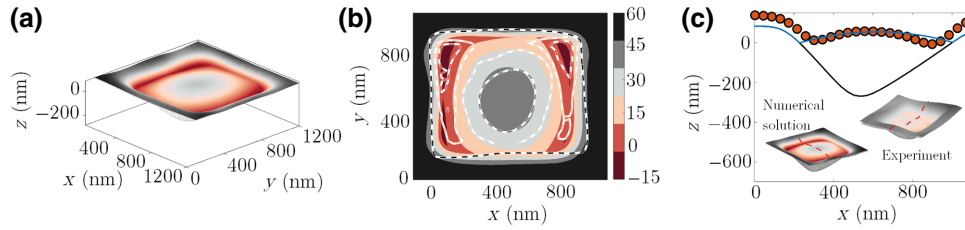


FIG. 5. Simulated vs experimental dewetted profiles in the three-dimensional case, in the case of a  $1.1\text{-}\mu\text{m}$ -period-inverted pyramid pattern with  $850\text{-nm}$  pyramid base. (a) Three-dimensional visualization of the simulated dewetted profile. (b) Comparison of the numerical (colored isocontours) and experimental (dashed isocontours) dewetted profiles. (c) Comparison along one section of the simulated dewetted profile (solid blue line) with the experimental AFM dewetted profile (orange dots).

period  $1.1\ \mu\text{m}$ , thickness  $60\ \text{nm}$ , see Fig. 5). Remarkably, the model reproduces with accuracy the experimental height profile over the range of thicknesses considered in this work. It is interesting to note that the proposed framework also predicts a thickness threshold,  $h_{\text{crit}}$ , above which the final film equilibrium, upon simulation, leads to a flat film covering the full substrate, instead of isolated droplets, as shown in Fig. S3 within the Supplemental Material [52] for an initial thickness of  $h_i = 100\ \text{nm}$ . This ultimately leads to dewetting according to nucleation and growth holes with a random location instead of a well-prescribed location. The random nucleation and growth of holes are observed experimentally at around  $80\ \text{nm}$  (contact angle  $64.5^\circ$ ), which is well in line with the results of Fig. S3 within the Supplemental Material [52]. These results highlight the relevance of continuum-mechanics schemes, even at thicknesses that become comparable with atomistic length scales.

Given that the rearrangement of the material is fundamentally linked to the increase in local curvature, the influence of the radius of curvature of the edges of the underlying substrate on the final structures is further investigated (see Fig. S4 within the Supplemental Material [52]). Simulated transitory states may differ depending on the pyramid-base edge curvature, giving rise, in some cases, to pinning behavior. Nevertheless, the final dewetted architectures appear to be independent of pyramid edge curvature for sufficiently long simulation times.

A peculiarity of dewetting in such pyramid arrays pertains to the distribution of material in the final microstructure, which widely varies, depending on the spacing-to-period ratio. In Figs. 6(a)–6(c), the final volume inside the pyramid,  $V_{\text{in}}$ , over the total volume,  $V_{\text{tot}}$ , is evaluated by simulation in the two-dimensional case. In the case where the final pyramid volume would be solely constituted from the material initially deposited inside the trench, the pyramid volume should be constant with spacing. This would therefore impose a well-defined law, referred to in this work as volume conservation, according to which the initial volume inside and outside the periodic trenches is conserved:  $V_{\text{in}}/V_{\text{tot}} = h_i W/h_i P$  and

$V_{\text{out}}/V_{\text{tot}} = [h_i(P - W)]/h_i P$ . Both the experimental and numerical results show a clear deviation from the volume-conservation law at low values of the spacing-to-period ratio, labeled  $S$ , where the film located at the pyramid edges is preferentially pulled inside the pyramid [see Figs. 6(c) and 6(d)]. On the contrary, at larger spacing-to-period ratios, the ratio  $V_{\text{in}}/V_{\text{tot}}$  follows closely the volume conservation law. While the thickness dependence does not appear in the experimental volume analysis, the deviating trend is observed for all configurations investigated. At reduced spacing, the absence of droplets between pyramids (“mesa”) is observed for spacing-to-period ratios up to  $0.35$ , while, at very large spacing, the instability in the top plane gives rise to a double distribution in size, and thus, to a new architecture. To provide the reader with an overview of the architectures as a function of spacing and thickness, a diagram is provided in Fig. 6(e). Additional SEM images, showing the full structural transition with the thickness and spacing-to-period ratio, are provided in Fig. S5 within the Supplemental Material [52]. All microstructures observed in the present study are reminiscent of the Wenzel state on textured surfaces [54]. This observation can be directly related to the choice of deposition method, which, in the present case, is thermal evaporation under vacuum.

### C. Application in photonics: Phase control

We now turn to exploit this in-depth understanding and control of template dewetting to realize advanced optical metasurfaces. Ordered high-index nanoparticles bear particular importance for metasurfaces or metagratings, which enable the tailoring of the phase, amplitude, and polarization of light over reduced thicknesses, in stark contrast to current bulky optical components [55,56]. By engineering the coupling between the various Mie modes through geometry, recent works have demonstrated the ability to tailor the emitted phase. These so-called Huygens meta-atoms provide control over the phase, covering the full  $0\text{--}2\pi$  range, hence enabling arbitrarily tailored phase profiles [57–59]. Several demonstrations based on this

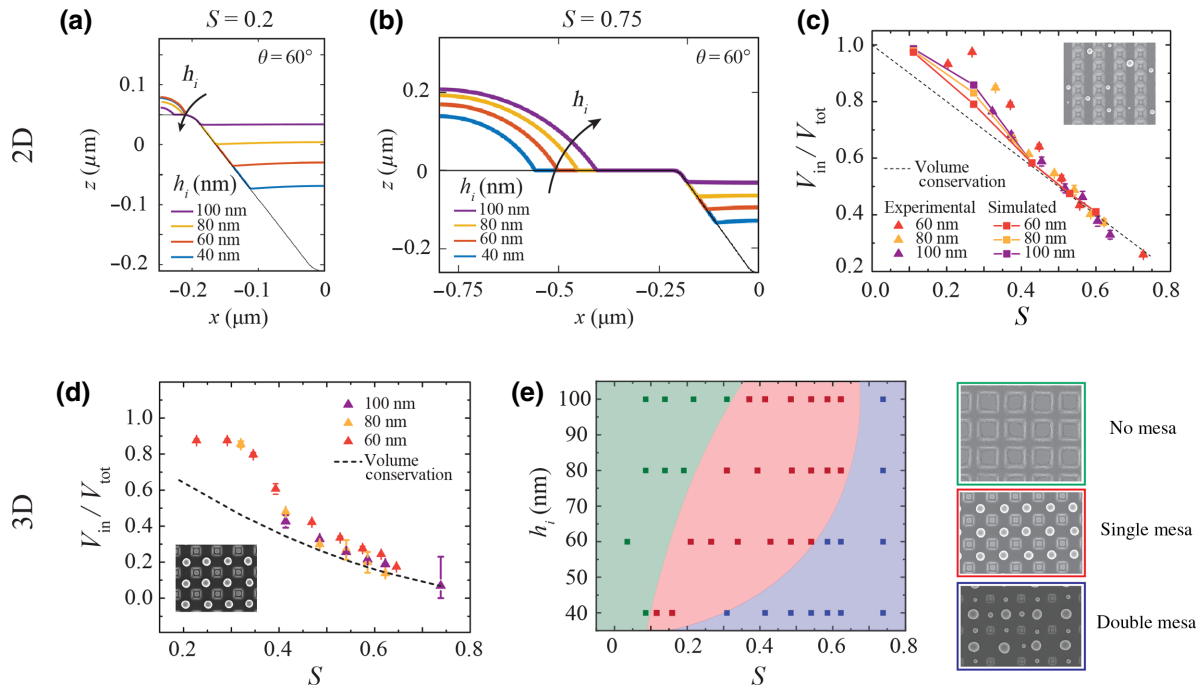


FIG. 6. Distribution of film material upon dewetting. Simulated two-dimensional final film profiles upon dewetting for spacing-to-period ratios,  $S$ , of  $S = 0.2$  (a) and  $S = 0.75$  (b). Mesa particle size grows with film thickness for  $S = 0.75$ ; trend is reversed for  $S = 0.2$ . (c)  $V_{in}/V_{tot}$  in the case of two-dimensional templates. Colors indicate the initial film thickness. Orange, 60 nm; yellow, 80 nm; purple, 100 nm. (d) Experimental pyramid-volume-to-total-volume ratio in the case of an inverted-pyramid array with increasing spacing. (e) Structure diagram associated with inverted pyramids with varying spacing-to-period ratio and film thickness. Film material is composed of  $As_2Se_3$  on a plasma-treated Ormocomp substrate. Graph's background coloring qualitatively indicates the microstructural stability domains.

concept have been implemented, such as lensing. Nevertheless, achieving full control over phase imposes stringent requirements, since geometrical changes of a few tens of nanometers may have a significant impact on the optical response. Given the high accuracy, in terms of both position and spacing in template dewetting, quasi-three-dimensional structures present remarkable opportunities, in terms of phase modulation [7,59].

Let us now focus on the optical properties arising from periodic architectures based on inverted pyramids with increasing spacing along the two principal axes (single-mesa architecture in Fig. 6). We proceed to evaluate the meta-assembly spectrum in reflection for three distinct period values ( $P = 1270, 1440, 1550$  nm), keeping the pyramid base constant at 850 nm [see Fig. 7]. The experimental spectra of line arrays are further compared with the equivalent simulated shapes. The simulated geometrical shapes rely on both experimental equilibrium contact angles and the volume-conservation criterion, which together define a relationship between evaporated film thickness and line width. Since the system is highly sensitive to slight geometrical changes, as low as 10 nm, experimental and simulated reflection spectra appear relatively well in agreement. We now turn to the evolution in phase

for a range of periods from 1200 to 1500 nm. Interestingly, interference between the various individual particle Mie modes cumulate to yield a cumulative phase shift over the complete  $2\pi$ -phase range at  $\lambda = 784$  nm. The phase shift is gradual, spanning from 1200 to 1500 nm, hence allowing for phase control with experimentally attainable accuracies. One can also note a particularly sharp  $2\pi$ -phase shift occurring for periods around 1410 nm, which highlights the sensitivity of imparted phase on geometrical parameters.

A similar study for two-dimensional templates (see Fig. S6 within the Supplemental Material [52]) also yields a coherent match between experimental and simulated spectra. Considering the spacing-to-period ratios studied here, we can resort solely to the volume conservation hypothesis to link thickness with resulting geometrical parameters. This allows for a completely “blind” implementation of geometry in finite-difference time-domain (FDTD) simulation software, which bears significant advantages in terms of design scalability. The phase profile shows extended phase-control possibilities around 684 nm (see Fig. S6 within the Supplemental Material [52]), with an extended range of periods to tune the phase, spanning from 1400 to 1900 nm.

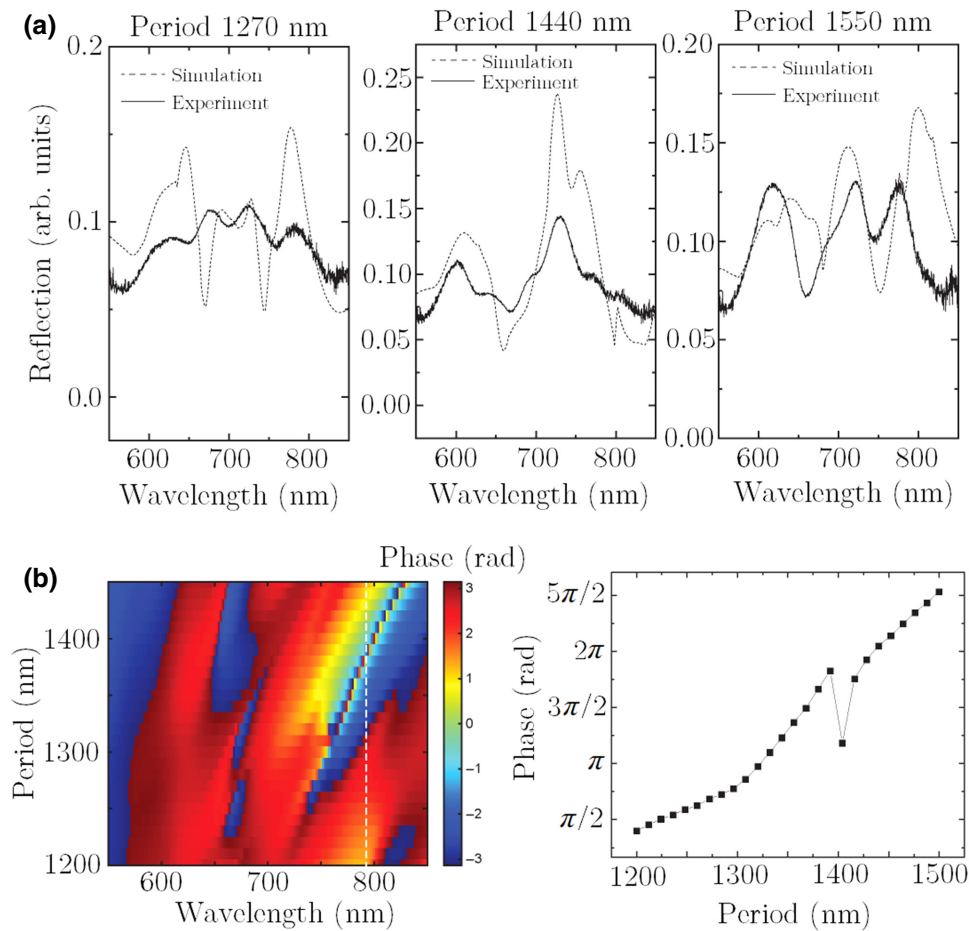


FIG. 7. Phase control for meta-gratings. (a) Simulated (dashed line) and experimental (solid line) reflection spectra for three periodicities ( $P = 1270, 1440,$  and  $1550$  nm) and fixed pyramid size of  $850$  nm. Spectra are not normalized with their own maximum but compared in absolute value. (b) Left, color map representing the phase imparted by the quasi-three-dimensional (3D) resonating structure to the outbound beam, as a function of period and wavelength. Pyramid width,  $W$ , is fixed at  $850$  nm. Right, plot representing phase as a function of period at  $784$  nm, corresponding to the white dashed line reported in the plot on the left.

### III. CONCLUSION

We introduce a modeling framework for the dewetting of films over a templated substrate based on a precursor-film approach. By resorting to a Lennard-Jones potential model, solutions to the dewetting problem are identified. Comparisons between final simulated and experimental film profiles show quantitative agreement, thereby providing a predictive model for the fabrication of nanostructures via dewetting on templated substrates. Finally, we demonstrate how this fine understanding of the resulting geometries paves the way for wave-front control in quasi-three-dimensional architectures. Further works to accelerate the convergence of the model in 3D would allow for an end-to-end framework that combines three-dimensional dewetting models with photonic simulation tools, enabling the direct simulation of the optical properties of a dewetted pattern based on simple input parameters (mainly initial thickness and pattern profile). This would thereby significantly expand the opportunities for the fabrication of self-assembled nanostructures, with a precision comparable to that of advanced lithographic processes. These considerations find immediate applications in the context of metasurfaces and beyond in the field of nanophotonics.

### ACKNOWLEDGMENTS

The authors would like to thank the scientific staff from the Center of Micro and nanotechnology (CMi) and the Center for electron microscopy (CIME) at EPFL for help and insightful discussions. The authors further thank Kuang-Yu Yang from the Nanophotonics and Metrology Laboratory at EPFL for help with the reflection measurements. The authors hereby thank the financial contributors to this work, namely, the European Research Council (Starting Grant No. 679211, “Flowtonics”) and the Swiss National Science Foundation (Grant No. 200021\_178971).

### APPENDIX A: SAMPLE FABRICATION

Chalcogenide thin films ( $\text{Se}$ ,  $\text{As}_2\text{Se}_3$ ) are first thermally evaporated (UNIVEX 350, Oerlikon, Germany) onto three types of substrate: two UV-curable polymers (Ormocomp®, Ormostamp®), which are well suited for nanoimprint lithography, and a pure silica texture obtained by a sol-gel process. We evaporate the films on both textured and nontextured regions to later compare these two relative situations. The film thickness is monitored during evaporation using a quartz crystal (Inficon, Switzerland). Film viscosity is dramatically reduced upon annealing



above the glass transition temperature, and enhanced chain mobility allows for dewetting to occur. Dewetting is performed by placing the sample for 30 min over a hotplate at 200 °C. We verify the steadiness of the patterns by both qualitative and quantitative comparison of the dewetted structures at different times using both scanning electron and atomic force microscopy, observing steady patterns for all studied cases upon 20 min of annealing.

## APPENDIX B: CONTACT-ANGLE MEASUREMENTS

To experimentally determine contact angles, we proceed to dewet evaporated thin films. This is triggered by thermal annealing above the glass transition temperature of the film for extended durations, e.g., twice the time required to observe a stable microstructure based on top-view observations using optical microscopy. To avoid uncertainty associated with tip shape in atomic force microscopy (AFM), we proceed instead to measure contact angles by cross-section imaging using scanning electron microscopy (SEM). Cross sections of the obtained samples are then prepared using liquid nitrogen. All SEM samples are coated with a 10-nm carbon film. The SEM images are taken with a Zeiss Merlin field-emission SEM instrument equipped with a GEMINI II column operating at 1.0 kV with a probe current of 70 pA. Contact angles are extracted using image analysis to accurately extract the contact angles (Image J, Contact Angle Module).

## APPENDIX C: NUMERICAL SIMULATIONS

The numerical implementation of lubrication Eq. (1) with complete curvature, together with interface-potential Eq. (2), is performed in the finite-element solver COMSOL Multiphysics. The equations are discretized for the variables  $(h, \kappa)$ . We consider quadratic Lagrangian elements for spatial discretization, with a triangular nonstructured grid for the two-dimensional case. We exploit the built-in backward differentiation formula algorithm for time marching, setting a tolerance of  $10^{-5}$ . Numerical convergence is achieved by performing several simulations with  $h_s = 0$  and verifying the convergence of the contact angle to the desired value.

As outlined above, the approach for the simulation of experimental conditions is based on the choice of the contact angle and the retrieval of the equilibrium thickness and Born coefficient. The Lennard-Jones potential reads

$$\Pi = -\frac{\partial\varphi}{\partial h} = \frac{8B}{h^9} - \frac{A}{6\pi h^3}, \quad (\text{C1})$$

where the Hamaker constant,  $A$ , is estimated based on Lifschitz theory. Following Ref. [46], the macroscopic contact

angle at equilibrium is given by

$$1 + \tan^2\theta = \left[ \frac{\varphi(h_{\text{eq}})}{\gamma} + 1 \right]^{-2}, \quad (\text{C2})$$

where  $\varphi(h_{\text{eq}})$  is the equilibrium potential, obtained by imposing  $\varphi'(h_{\text{eq}}) = 0$ , where  $h_{\text{eq}}$  is the equilibrium thickness (i.e., precursor-film thickness). Once the contact angle is fixed, the previous relation (C2) gives a unique value of the equilibrium potential in the range  $[0^\circ, 90^\circ]$ , with  $A > 0$ . The value of the equilibrium potential can be used to evaluate the equilibrium thickness. Deriving Eq. (2) with respect to  $h$  and evaluating it at equilibrium thickness,  $h_{\text{eq}}$ , yields

$$0 = -\frac{8B}{h_{\text{eq}}^9} + \frac{A}{6\pi h_{\text{eq}}^3}, \quad (\text{C3})$$

$$h_{\text{eq}} = \left( \frac{48\pi B}{A} \right)^{1/6} \rightarrow \frac{B}{A} = \frac{h_{\text{eq}}^6}{48\pi}. \quad (\text{C4})$$

Substituting  $B/A$  in Eq. (2), at the equilibrium thickness, we have

$$\varphi(h_{\text{eq}}) = \varphi_{\text{eq}} = -\frac{A}{16\pi h_{\text{eq}}^2}, \quad (\text{C5})$$

where  $\varphi(h_{\text{eq}})$  is associated with a unique contact angle between  $0^\circ$  to  $90^\circ$ , according to Eq. (4). From Eqs. (C4) and (C5), we can thus evaluate  $h_{\text{eq}}$  and  $B = (B/A)A$ , with the knowledge of  $\varphi_{\text{eq}}$  and  $A$ .

## APPENDIX D: EVALUATION OF THE HAMAKER CONSTANT USING LIFSCHITZ THEORY AND TYPICAL VALUES

The Hamaker constant,  $A$ , quantifies the imbalance in van der Waals forces as two interfaces are brought closer to each other. Lifschitz [42] developed a theory to account for the collective interactive forces between macroscopic particles from quantum-field theory that related the interaction energy with the interparticle distance. The interactions between particles are relative to macroscopic properties: the dielectric constant,  $\epsilon$ , and the refractive index,  $n$ . The

TABLE I. Refractive indices in the visible region of typical materials involved in the present study.

Material	Refractive index	Details	Ref.
SiO <sub>2</sub>	1.45	@550 nm, fused silica	[60]
As <sub>2</sub> Se <sub>3</sub>	3.5	@550 nm	Ellipsometry measurement
Ormocomp (OC)	1.52	@589 nm	From fabricant

Hamaker constant of a system made of a liquid film (3) placed between a gas or immiscible liquid (2) and a solid (1) can be estimated by considering the overall system energy, which includes (i) permanent polar dipole

interactions (Keesom and Debye molecular forces) and (ii) induced dipole interactions (London dispersion forces), which depend on the orbiting electron frequency,  $\nu$ , and the refractive index,  $n$ , of media [45]:

$$A = A_{\nu=0} + A_{\nu>0},$$

$$A \approx \frac{3kT}{4} \left[ \frac{\varepsilon_1(0) - \varepsilon_3(0)}{\varepsilon_1(0) + \varepsilon_3(0)} \right] \left[ \frac{\varepsilon_2(0) - \varepsilon_3(0)}{\varepsilon_2(0) + \varepsilon_3(0)} \right] + \frac{3h\nu_e}{8\sqrt{2}} \frac{(n_1^2 - n_3^2)(n_2^2 - n_3^2)}{(n_1^2 + n_3^2)^{1/2}(n_2^2 + n_3^2)^{1/2}[(n_1^2 + n_3^2)^{1/2} + (n_2^2 + n_3^2)^{1/2}]},$$

where  $\nu_e$  is the principal UV-absorption frequency ( $\sim 3 \times 10^{15}$  Hz),  $n_i$  refers to the visible real refractive index of species  $i$ , and  $h$  is the Planck constant. Unless strongly polar molecules are involved, the first term can be safely neglected [45].

Based on Lifschitz theory and the refractive indices provided in Table I, the following Hamaker constants are obtained:

$$A_{\text{OC-As}_2\text{Se}_3\text{-air}} = 5.7 \times 10^{-19} \text{ J},$$

$$A_{\text{SiO}_2\text{-As}_2\text{Se}_3\text{-air}} = 5.9 \times 10^{-19} \text{ J}.$$

## APPENDIX E: ATOMIC FORCE MICROSCOPY MEASUREMENTS

All AFM measurements are performed at room temperature (largely below the glass transition temperature of  $\text{As}_2\text{Se}_3$ , identified at 120 °C), which ensures that  $\text{As}_2\text{Se}_3$  is completely solid during scanning. Atomic force microscopy images are collected in amplitude modulation mode on a commercial Cypher S system (Asylum Research/Oxford Instruments, Santa Barbara, CA). Two kinds of cantilevers are used: the sensitivity of Asytec cantilevers (Asylum Research) is evaluated from force curves and the spring constant is measured from their thermal spectra, while AC240TS cantilevers (Asylum Research) are calibrated using the built-in GetReal automated probe calibration procedure. The cantilevers are driven acoustically. Using Gwyddion postprocessing software, a polynomial plane leveling of second order is achieved followed by scar removal using the in-built functions. We use the smoothed profiles for an overall comparison of the profiles with numerical simulations. Uncertainties linked to the sharp slope profiles near the triple line are very localized and do not alter the overall match between the simulated and measured profiles.

## APPENDIX F: REFLECTION MEASUREMENTS

Reflection spectra are characterized using a Nikon Optiphot 200 inspection microscope (10 $\times$ , NA=0.25 objective). A CCD camera (Digital Sight DS-2Mv, Nikon) is used to record the images of the sample, and the images are processed with NIS-Elements F3.2 software. The spectra are characterized with a visible-near-IR spectroscopy system based on an inverted optical microscope (Olympus IX-71) coupled to a spectrometer (Jobin Yvon Horiba Triax 550). The sample is illuminated using a halogen white-light source focused onto the sample using an objective (20 $\times$ , NA=0.4). The reflected light is collected through the same objective and recorded using a spectrometer. The reflected intensity is normalized by the spectrum of the lamp obtained by reflection measurements with a silver mirror (Thorlabs PF 10-03-P01). A polarizer (WP25M-UB, Thorlabs) is used to set linear-polarized-light illumination for both reflection and transmission measurements.

## APPENDIX G: OPTICAL SIMULATIONS

The built-in  $S$ -parameter analyzer from the FDTD solver package (Lumerical) is used to extract complex transmission and reflection coefficients. This analysis script calculates the following quantities: (i) fraction of transmitted and reflected power, using 2D monitors and transmission function; and (ii) complex reflection and transmission coefficients ( $S$  parameters). The latter coefficients are calculated from the amplitude and phase of the fields, as measured by the point monitors. This technique assumes that the system is single mode (only one grating order) and that the monitors are far away enough from the structure so that the fields are propagating like a plane wave. A phase correction is also necessary to compensate for the phase that accumulates as fields propagate through the background medium from the source to the metamaterial and from the metamaterial to the monitors. The provided phase, therefore, corresponds to the difference in phase accumulated over the metamaterial layer.

- [1] P. Gilles de Genes, F. Brochart-Wyart, and D. Quéré, *Capillarity and Wetting Phenomena: Drops, Bubbles, Pearls, Waves* (Springer International Publishing, Cham, 2004).
- [2] G. Reiter, Dewetting of Thin Polymer Films, *Phys. Rev. Lett.* **68**, 75 (1992).
- [3] R. Xie, A. Karim, J. F. Douglas, C. C. Han, and R. A. Weiss, Spinodal Dewetting of Thin Polymer Films, *Phys. Rev. Lett.* **81**, 1251 (1998).
- [4] S. C. Thickett, C. Neto, and A. T. Harris, Biomimetic surface coatings for atmospheric water capture prepared by dewetting of polymer films, *Adv. Mater.* **23**, 3718 (2011).
- [5] P. Chakrabarty, A. Ghorai, S. K. Ray, and R. Mukherjee, Polymer thin-film dewetting-mediated growth of wettability-controlled titania nanorod arrays for highly responsive, water-stable self-powered UV photodetectors, *ACS Appl. Electron. Mater.* **2**, 2895 (2020).
- [6] N. Bhandaru, G. Kaur, A. Panjla, and S. Verma, Spin coating mediated morphology modulation in self assembly of peptides, *Nanoscale* **13**, 8884 (2021).
- [7] T. D. Gupta, L. Martin-Monier, W. Yan, A. Le Bris, T. Nguyen-Dang, A. G. Page, K.-T. Ho, F. Yesilköy, H. Altug, and F. Sorin, Self-assembly of nanostructured glass metasurfaces via templated fluid instabilities, *Nat. Nanotech.* **14**, 320 (2019).
- [8] G. Lu, W. Li, J. Yao, G. Zhang, B. Yang, and J. Shen, Fabricating ordered two-dimensional arrays of polymer rings with submicrometer-sized features on patterned self-assembled monolayers by dewetting, *Adv. Mater.* **14**, 1049 (2002).
- [9] E. Meyer and H.-G. Braun, Controlled dewetting processes on microstructured surfaces—a new procedure for thin film microstructuring, *Macromol. Mater. Eng.* **276–277**, 44 (2000).
- [10] N. Bhandaru, A. Das, N. Salunke, and R. Mukherjee, Ordered alternating binary polymer nanodroplet array by sequential spin dewetting, *Nano Lett.* **14**, 7009 (2014).
- [11] S. Roy and R. Mukherjee, Ordered to isotropic morphology transition in pattern-directed dewetting of polymer thin films on substrates with different feature heights, *ACS Appl. Mater. Interfaces* **4**, 5375 (2012).
- [12] K. Kargupta and A. Sharma, Templating of Thin Films Induced by Dewetting on Patterned Surfaces, *Phys. Rev. Lett.* **86**, 4536 (2001).
- [13] K. Kargupta and A. Sharma, Dewetting of thin films on periodic physically and chemically patterned surfaces, *Langmuir* **18**, 1893 (2002).
- [14] C. V. Thompson, Solid-state dewetting of thin films, *Annu. Rev. Mater. Res.* **42**, 399 (2012).
- [15] A. Verma and A. Sharma, Self-organized nano-lens arrays by intensified dewetting of electron beam modified polymer thin-films, *Soft Matter* **7**, 11119 (2011).
- [16] R. Seemann, M. Brinkmann, E. J. Kramer, F. F. Lange, and R. Lipowsky, Wetting morphologies at microstructured surfaces, *Proc. Natl Acad. Sci.* **102**, 1848 (2005).
- [17] A. Le Bris, F. Maloum, J. Teisseire, and F. Sorin, Self-organized ordered silver nanoparticle arrays obtained by solid state dewetting, *Appl. Phys. Lett.* **105**, 203102 (2014).
- [18] A. L. Giermann and C. V. Thompson, Solid-state dewetting for ordered arrays of crystallographically oriented metal particles, *Appl. Phys. Lett.* **86**, 121903 (2005).
- [19] F. Leroy, Ł. Borowik, F. Cheynis, Y. Almadori, S. Curiotto, M. Trautmann, J. C. Barbé, and P. Müller, How to control solid state dewetting: A short review, *Surf. Sci. Rep.* **71**, 391 (2016).
- [20] A. Das and R. Mukherjee, Feature size modulation in dewetting of nanoparticle-containing ultrathin polymer films, *Macromolecules* **54**, 2242 (2021).
- [21] D. Kim, A. L. Giermann, and C. V. Thompson, Solid-state dewetting of patterned thin films, *Appl. Phys. Lett.* **95**, 251903 (2009).
- [22] R. V. Zucker, PhD Thesis, Massachusetts Institute of Technology, 2015.
- [23] P. Volodin and A. Kondyurin, Dewetting of thin polymer film on rough substrate: I. Theory, *J. Phys. D App. Phys.* **41**, 065306 (2008).
- [24] P. Volodin and A. Kondyurin, Dewetting of thin polymer film on rough substrate: II. Experiment, *J. Phys. D: App. Phys.* **41**, 065307 (2008).
- [25] E. Pauliac-Vaujour, A. Stannard, C. P. Martin, M. O. Blunt, I. Nottingher, P. J. Moriarty, I. Vancea, and U. Thiele, Fingering Instabilities in Dewetting Nanofluids, *Phys. Rev. Lett.* **100**, 176102 (2008).
- [26] G. Yosef and E. Rabani, Self-assembly of nanoparticles into rings: A lattice-gas model, *J. Phys. Chem. B* **110**, 20965 (2006).
- [27] P. C. Ohara and W. M. Gelbart, Interplay between hole instability and nanoparticle array formation in ultrathin liquid films, *Langmuir* **14**, 3418 (1998).
- [28] E. Rabani, D. R. Reichman, P. L. Geissler, and L. E. Brus, Drying-mediated self-assembly of nanoparticles, *Nature* **426**, 271 (2003).
- [29] K. Mahady, S. Afkhami, J. Diez, and L. Kondic, Comparison of Navier-Stokes simulations with long-wave theory: Study of wetting and dewetting, *Phys. Fluids* **25**, 112103 (2013).
- [30] W. Jiang, W. Bao, C. V. Thompson, and D. J. Srolovitz, Phase field approach for simulating solid-state dewetting problems, *Acta Mater.* **60**, 5578 (2012).
- [31] C. A. Hartnett, K. Mahady, J. D. Fowlkes, S. Afkhami, L. Kondic, and P. D. Rack, Instability of nano-and microscale liquid metal filaments: Transition from single droplet collapse to multidroplet breakup, *Langmuir* **31**, 13609 (2015).
- [32] S. Afkhami and L. Kondic, On the dewetting of liquefied metal nanostructures, *J. Eng. Math.* **94**, 5 (2015).
- [33] K. Mahady, S. Afkhami, and L. Kondic, A volume of fluid method for simulating fluid/fluid interfaces in contact with solid boundaries, *J. Comp. Phys.* **294**, 243 (2015).
- [34] D. Bonn, J. Eggers, J. Indekeu, J. Meunier, and E. Rolley, Wetting and spreading, *Rev. Mod. Phys.* **81**, 739 (2009).
- [35] K. Mahady, S. Afkhami, and L. Kondic, A numerical approach for the direct computation of flows including fluid-solid interaction: Modeling contact angle, film rupture, and dewetting, *Phys. Fluids* **28**, 062002 (2016).
- [36] A. Oron, S. H. Davis, and S. G. Bankoff, Long-scale evolution of thin liquid films, *Rev. Mod. Phys.* **69**, 931 (1997).
- [37] L. Kondic, A. G. González, J. A. Diez, J. D. Fowlkes, and P. Rack, Liquid-state dewetting of pulsed-laser-heated nanoscale metal films and other geometries, *Annu. Rev. Fluid Mech.* **52**, 235 (2020).

- [38] J. Becker, G. Grün, R. Seemann, H. Mantz, K. Jacobs, K. R. Mecke, and R. Blossey, Complex dewetting scenarios captured by thin-film models, *Nat. Mater.* **2**, 59 (2003).
- [39] R. Seemann, S. Herminghaus, and K. Jacobs, Dewetting Patterns and Molecular Forces: A Reconciliation, *Phys. Rev. Lett.* **86**, 5534 (2001).
- [40] V. S. Mitlin, Dewetting of solid surface: Analogy with spinodal decomposition, *J. Colloid Interface Sci.* **156**, 491 (1993).
- [41] A. Sharma and R. Khanna, Pattern Formation in Unstable Thin Liquid Films, *Phys. Rev. Lett.* **81**, 3463 (1998).
- [42] E. M. Lifschitz, The theory of molecular attractive forces between solids, *Exper. Theoret. Phys. USSR* **29**, 94 (1955).
- [43] C. Maldarelli, R. K. Jain, and I. B. Ivanov, Stability of symmetric and unsymmetric thin liquid films to short and long wavelength perturbations, *J. Colloid Inter. Sci.* **78**, 1 (1980).
- [44] I. B. Ivanov, *Thin Liquid Films, Ed.* (Marcel Dekker, Inc., New York, 1988).
- [45] J. Israelichvili, *Intermolecular and Surface Forces* (Academic Press, San Diego, 2011).
- [46] A. Sharma, Equilibrium contact angles and film thicknesses in the apolar and polar systems: Role of intermolecular interactions in coexistence of drops with thin films, *Langmuir* **9**, 3580 (1993).
- [47] S. D. R. Wilson, The drag-out problem in film coating theory, *J. Eng. Math.* **16**, 209 (1982).
- [48] G. Lerisson, P. G. Ledda, G. Balestra, and F. Gallaire, Instability of a thin viscous film flowing under an inclined substrate: Steady patterns, *J. Fluid. Mech.* **898**, A6 (2020).
- [49] P. G. Ledda, G. Lerisson, G. Balestra, and F. Gallaire, Instability of a thin viscous film flowing under an inclined substrate: The emergence and stability of rivulets, *J. Fluid Mech.* **904**, A23 (2020).
- [50] E. Jambon-Puillet, P. G. Ledda, F. Gallaire, and P. T. Brun, Drops on the Underside of a Slightly Inclined Wet Substrate Move Too Fast to Grow, *Phys. Rev. Lett.* **127**, 044503 (2021).
- [51] P. G. Ledda and F. Gallaire, Secondary instability in thin film flows under an inclined plane: Growth of lenses on spatially developing rivulets, *Proc. R. Soc. A.* **477**, 20210291 (2021).
- [52] See the Supplemental Material at <http://link.aps.org/supplemental/10.1103/PhysRevApplied.16.034025> for additional experimental and numerical results.
- [53] P. G. Ledda, G. Balestra, G. Lerisson, B. Scheid, M. Wyart, and F. Gallaire, Hydrodynamic-driven morphogenesis of karst draperies: Spatio-temporal analysis of the two-dimensional impulse response, *J. Fluid Mech.* **910**, A53 (2021).
- [54] D. Murakami, H. Jinnai, and A. Takahara, Wetting transition from the Cassie–Baxter state to the Wenzel state on textured polymer surfaces, *Langmuir* **30**, 2061 (2014).
- [55] N. Yu and F. Capasso, Flat optics with designer metasurfaces, *Nat. Mater.* **13**, 139 (2014).
- [56] G. Li, S. Zhang, and T. Zentgraf, Nonlinear photonic metasurfaces, *Nat. Rev. Mater.* **2**, 17010 (2017).
- [57] M. Decker, I. Staude, M. Falkner, J. Dominguez, D. N. Neshev, I. Brener, T. Pertsch, and Y. S. Kivshar, High-efficiency dielectric Huygens’ surfaces, *Adv. Opt. Mater.* **3**, 813 (2015).
- [58] A. Leitis, A. Heßler, S. Wahl, M. Wuttig, T. Taubner, A. Tittl, and H. Altug, All-dielectric programmable Huygens’ metasurfaces, *Adv. Funct. Mater.* **30**, 1910259 (2020).
- [59] Y. Ra’di, D. L. Sounas, and A. Alu, Metagratings: Beyond the Limits of Graded Metasurfaces for Wave Front Control, *Phys. Rev. Lett.* **119**, 067404 (2017).
- [60] I. H. Malitson, Interspecimen comparison of the refractive index of fused silica, *J. Opt. Soc. Am.* **55**, 1205 (1965).